Proc. of the 15th Int. Workshop on Slow Positron Beam Techniques and Applications, Prague, September 2–6, 2019

Quenched-in Vacancies and Hardening of Fe–Al Intermetallics

I. Prochazka[a,*], T. Vlasak[a], J. Cizek[a], F. Lukac[a,b], M.O. Liedke[c], W. Anwand[c], Y. Jiraskova[d] and D. Janickovic[e]

[a]Faculty of Mathematics and Physics, Charles University, V Holesovickach 2, 180 00 Praha 8, Czech Republic
[b]Institute of Plasma Physics of the Czech Academy of Sciences, Za Slovankou 3, 182 00 Praha 8, Czech Republic
[c]Institute of Radiation Physics, Helmholtz Zentrum Dresden-Rossendorf, Bautzner Landstr. 400, 01328 Dresden, Germany
[d]Institute of Physics of Materials, Academy of Science of the Czech Republic, Žižkova 513/22, Brno 61662, Czech Republic
[e]Institute of Physics, Slovak Academy of Science, Dubravska cesta 9, Bratislava 84511, Slovak Republic

The role of vacancies in hardening of Fe–Al intermetallic alloys were studied in the present work for a wide range of Al concentrations from 20 to 50 at%. The alloys quenched from 1000 °C as well as those annealed subsequently at 520 °C for 1 h were subject to study. Slow-positron beam experiments combined with Vicker's microhardness tests were utilised. Hardness of Fe–Al alloys exhibited a somewhat complex dependence on Al content which could not be fully explained purely by consideration of intermetallic phases formed. This happens due to additional hardening effect caused by quenched-in vacancies. The concentrations of vacancies were estimated from positron back-diffusion data and found to rise for Al content above 25 at%. Correlation of vacancy concentrations with hardness data for the quenched and annealed alloys has revealed that hardening of alloys with a low Al content ($<$ 30 at%) is originated predominantly by anti-phase boundaries while hardening induced by quenched-in vacancies dominates for alloys with a higher Al content (30–50 at%).

DOI: 10.12693/APhysPolA.137.255

PACS/topics: positron annihilation spectroscopy, intermetallics, vacancies

1. Introduction

Iron–aluminum intermetallic alloys belong to attractive materials for industrial use. Particularly, they exhibit a low density, a high strength, and a good corrosion resistance. A low production cost of Fe–Al alloys is also advantageous.

Physical and functional properties of Fe–Al intermetallics are influenced by point defects and atomic ordering during slow cooling from high temperatures to room temperature (RT). The ordering appears to depend on Al content [1]. At ~ 1000 °C, the Fe–Al alloys exist in the disordered A2 phase. The Fe–Al alloys with a high Al concentration of 30–50 at% undergo transformation from the A2 phase to the partially ordered B2 structure when cooled down to RT. The Fe–Al alloys with a lower Al content (20–30 at%) pass first also through the A2 $\rightarrow$ B2 transition during cooling, but ordering continues with decreasing temperature reaching eventually the ordered D03 phase at RT. At high temperatures, the equilibrium concentrations of vacancies in Fe–Al alloys become as high as several at% [2]. Vacancies were for example shown to have a significant influence on hardness of these systems [3]. Thus comprehensive research on vacancies in Fe–Al alloys in a wide range of Al content is essential for complete understanding of physical and mechanical properties of these alloys.

The positron annihilation spectroscopy (PAS) has already been applied to defect studies of Fe–Al alloys several times [4–9]. The present work was aimed to expand knowledge of Fe–Al intermetallics and to gain more insight into the hardening role of quenched-in vacancies in Fe–Al alloys and effects of annealing, covering a wide range of Al concentrations (from $\approx$ 20 at% to $\approx$ 50 at%). The variable energy positron annihilation spectroscopy (VEPAS) was combined with Vickers microhardness (HV) measurements.

2. Experimental

2.1. Materials

A series of Fe–Al alloys, $Fe_{100-c_{Al}}Al_{c_{Al}}$, with Al concentrations, c_{Al} covering the range from 18 to 49 at% were prepared by arc melting of high-purity (99.99%) iron and aluminium in Ti-gettered argon atmosphere. Disk-shaped Fe–Al specimens ($\approx$ 15 mm diameter, $\approx$ 0.5 mm thickness) were cut from the cast ingot, annealed at 1000 °C for 1 h in evacuated quartz ampoules and promptly quenched into water at RT. The as-quenched specimens were first characterised by VEPAS or HV. Selected quenched specimens then underwent vacuum annealing at 520 °C for 1 h finished by quenching into RT water and followed by the measurements.

*corresponding author; e-mail: ivan.prochazka@mff.cuni.cz

2.2. Apparatus and data taking

VEPAS investigations were carried out using a ^{22}Na based continuous magnetically guided slow positron beam [10]. Positron energies E_+, covered the interval from 0.03 to 35 keV. The γ-spectra were measured with a HPGe spectrometer exhibiting an energy resolution of 1.06 keV (FWHM) at 511 keV. At least 2.5×10^5 counts were accumulated in each annihilation peak. The Doppler-broadened peak shapes were characterised through ordinary sharpness (S) and wing (W) parameters and normalised to values $S_0 = 0.5085 \pm 0.0010$ and $W_0 = 0.1004 \pm 0.0004$, to which measured S- and W-values were found to level for the quenched $Fe_{75}Al_{25}$ reference alloy above $E_+ \approx 20$ keV. The dependences S vs. E_+ were analysed by means of the VEPFIT code [11].

Vickers microhardness tests were carried out by applying 100 g load for 10 s using the STRUERS Duramin-2 micro-tester. Resulting HV-values were obtained by averaging at least 10 repeated tests.

3. Results And Discussion

3.1. VEPAS data

The dependences of S-parameters on positron energy E_+ measured for Fe–Al alloys in the present work, exhibited patterns illustrated in Fig. 1. For $E_+ < 2$ keV, a pronounced fall of the S-values with increasing E_+ was seen, which should be attributed to an oxide layer, that Fe–Al alloys are known to be covered with [8]. Above $E_+ \approx 2$ keV, gradual approach of S-parameters toward c_{Al}-specific bulk values, S_{bulk} (c_{Al}), was clearly visible, reflecting decreasing portion of positrons that could diffuse back to the surface, when E_+ was increased.

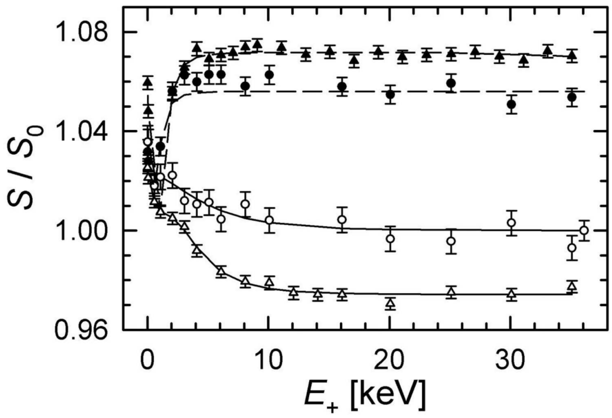

Fig. 1. Examples of measured S parameters, normalised as described in the text and plotted versus positron energy E_+: ○ — $Fe_{75}Al_{25}$, △ — $Fe_{74}Al_{26}$, ● — $Fe_{55}Al_{45}$, ▲ — $Fe_{51}Al_{49}$. Solid and dashed lines represent the VEPFIT modelled curves.

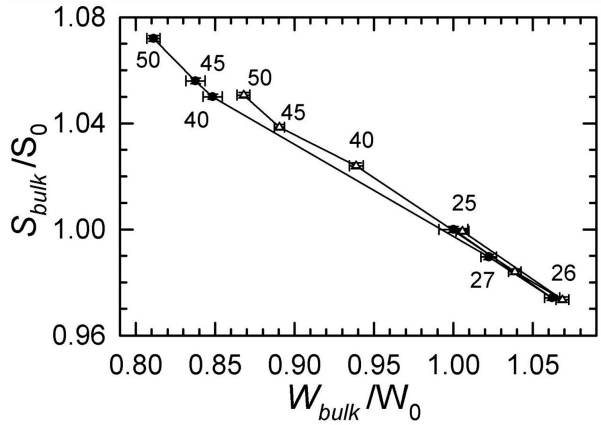

Fig. 2. S_{bulk} — W_{bulk} plot for quenched (●) and annealed (△) Fe–Al alloys. Numbers adjacent to data points denote Al concentration in at%. Lines were drawn just to guide eyes.

The measured $S(E_+)$ dependences were analysed by means of VEPFIT code [11]. In accordance with the observed shapes of these dependences, the fitting model included the two depth regions: (i) the thin (a few tens of nm) surface oxide layer, and (ii) the Fe–Al bulk. Below, we will focus on the bulk region characterised by shape parameters S_{bulk} and W_{bulk}, and the mean positron diffusion length $L_{+,\mathrm{bulk}}$. VEPFIT analysis of measured $W(E_+)$-dependences appeared to be less meaningful. W_{bulk} parameters could, however, be estimated by averaging measured W-values over the plateau region ($E_+ \geq 20$ keV). The bulk shape parameters were arranged in the S_{bulk}–W_{bulk} plot in Fig. 2. Roughly linear behaviour is featured by this plot for the quenched as well as annealed Fe–Al alloys, suggesting that the same defect species were dominating positron traps in the bulk region for all the Fe–Al alloys with Al content between 26 and 50 at%. For the quenched Fe–Al alloys, the evolution of S_{bulk}- and W_{bulk}-values with c_{Al} show a non-monotonicity around $c_{\mathrm{Al}} = 26$ at%, reaching the minimum in S_{bulk} (maximum in W_{bulk}) at $c_{\mathrm{Al}} = 26$ at%. Then, S_{bulk}-values were found to grow (W_{bulk} to decline) monotonically, see Fig. 2. For the annealed Fe–Al alloys, the evolution of the plot remains similar to the quenched alloys, however, the S_{bulk}-values are altogether lower (W_{bulk}-values higher) than corresponding data for the quenched alloys. The decrease in S_{bulk}-values for annealed alloys with respect to the quenched ones becomes more pronounced for $c_{\mathrm{Al}} > 40$ at%. The negative slope of the S_{bulk}–W_{bulk} line for the annealed alloys seems to be slightly higher than that for the quenched ones. In Fig. 3, $L_{+,\mathrm{bulk}}$-values obtained using VEPFIT analysis were plotted against the Al content. A decrease in diffusion lengths with increasing c_{Al} can be clearly seen in the figure, being more pronounced for the quenched alloys at higher Al content. The trends in S_{bulk}-, W_{bulk}- and $L_{+,\mathrm{bulk}}$-values displayed in Figs. 2 and 3 should be understood as a manifest of increasing role of defects in the bulk region of

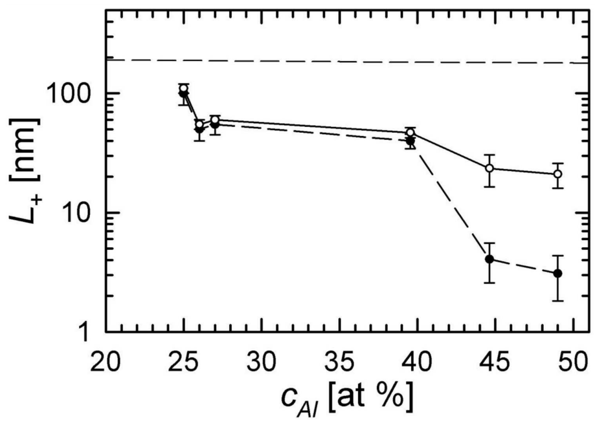

Fig. 3. Mean positron diffusion length, $L_{+,\mathrm{bulk}}$, in the Fe–Al bulk plotted against Al content, c_{Al} for quenched alloys (•) and annealed alloys (▲). $L_{+,B}$ (dashed line) stands for positron diffusion length in perfect lattice as estimated in [8]. Lines connecting the data points were drawn just to guide eyes.

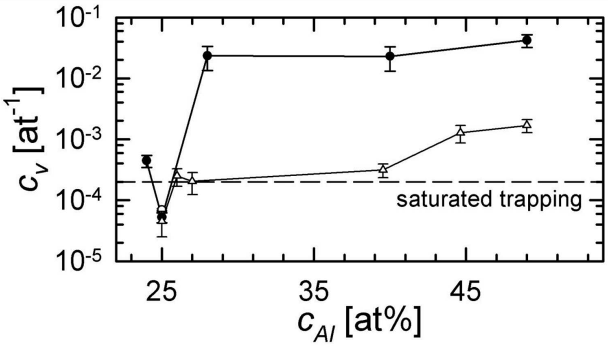

Fig. 4. Concentration of vacancies, c_{V}, displayed as function of Al content, c_{Al}: • — quenched alloys, △ — annealed alloys, ○ — LT result [8]. Vacancy concentrations were estimated from VEPAS experiments according to (1). Solid lines were drawn just to guide eyes. Dashed line stands for saturated trapping limit [8].

the Fe–Al alloys when Al concentration was rising up from $c_{\mathrm{Al}} \approx 26$ toward 50 at%. A similar conclusion could be also supported by our previous positron lifetime (LT) study of quenched Fe–Al alloys [8, 9] where the dominating positron traps were identified as the quenched-in Fe vacancies in the A-sublattice surrounded by Al neighbour atoms in the B-sublattice of which the number is growing with increasing Al content. A decrease of S_{bulk}-values after annealing the Fe–Al alloys is obviously a result of the recovery of the quenched-in vacancies.

The saturated positron trapping was observed by the LT technique in quenched Fe–Al alloys with $c_{\mathrm{Al}} > 26$ at% [8] and the LT method thus became ineffective to study changes in vacancy concentrations c_{V} in the alloys with higher Al content. Note that the saturated trapping limit could be estimated as $c_{V,lim} \approx 2\times10^{-4}$ at^{-1} [9]. The measurement of positron diffusion length, on the other hand, enables to estimate defect concentration in case of high defect densities in Fe–Al alloys as demonstrated in our previous studies [8, 9]. Assuming the Fe vacancy-like defects to be dominating positron traps, the procedure relies upon relation [11]

$$c_{\mathrm{V}} = \frac{1}{\nu_{\mathrm{V}}\tau_B}\left(\frac{L^2_{+,B}}{L^2_{+,\mathrm{bulk}}} - 1\right), \tag{1}$$

where $\nu_{\mathrm{V}} \approx 4\times10^{14}$ s^{-1} is the specific positron trapping rate for a Fe-vacancy [4], τ_B and $L_{+,B}$, respectively, stand for the free positron lifetime [6, 12] and the mean positron diffusion length [9] in a perfect Fe–Al lattice. Inserting $L_{+_{\mathrm{bulk}}}$-values of Fig. 3 into (1) one can calculate vacancy concentrations values. They were plotted against Al content in Fig. 4. Figure 4 includes also the c_{V} value for $c_{\mathrm{Al}} = 25$ deduced from the earlier LT data [8] for $Fe_{75}Al_{25}$, which turned out to closely coincide with the present VEPAS results. A substantial increase in the concentration of quenched-in vacancies with increased Al content was observed. In addition, a drop in the vacancy concentration in the annealed samples, compared to the quenched ones, is seen in Fig. 4, progressing markedly with increasing Al content above $c_{\mathrm{Al}} \approx 26$ at%.

3.2. HV data

Microhardness values measured for quenched and annealed Fe–Al alloys were collected in Fig. 5 as functions of Al concentration c_{Al}. Similarly to the VEPAS results, the data showed a non-monotonic behaviour: For quenched alloys, the HV-values first grew from $c_{\mathrm{Al}} \approx 20$ at% reaching a broad maximum at $c_{\mathrm{Al}} \approx 27$ at%. Then they exhibited a visible drop between $c_{\mathrm{Al}} \approx 27$ and ≈ 30 at%. Above $c_{\mathrm{Al}} \approx 30$ at%, another rise up of HV toward alloys with higher Al content was seen. After annealing at 520 °C per 1 h, only minor differences in hardness between quenched and annealed Fe–Al samples were found below $c_{\mathrm{Al}} = 27$ at%. Whereas, a remarkable decline of HV with respect to the quenched samples for Al content above ≈ 27 at% took place and this difference became gradually enlarged with increasing Al concentration, obviously reflecting an increasing vacancy concentration c_{V} revealed in this c_{Al} region by the VEPAS data of Sect. 3.1 as well as by earlier LT results [8]. Undoubtedly, such decrease should be due to annihilation of quenched-in vacancies during annealing. In annealed alloys, the HV-values were kept roughly stable between $C_{\mathrm{Al}} \approx 30$ and ≈ 40 at% indicating that applying of annealing at 520 °C for 1 h had been sufficient to anneal out a majority of quenched-in vacancies. Then a slight increase in HV was observed, see Fig. 5, resulting probably from contribution of triple defects (two aligned Fe vacancies in the A sublattice associated with an antisite Fe atom in the B sublattice). In fact, an increasing role of triple defects, which in Al-rich alloys is around $c_{\mathrm{Al}} \approx 50$ at%, was evidenced in our earlier positron lifetime measurements [8].

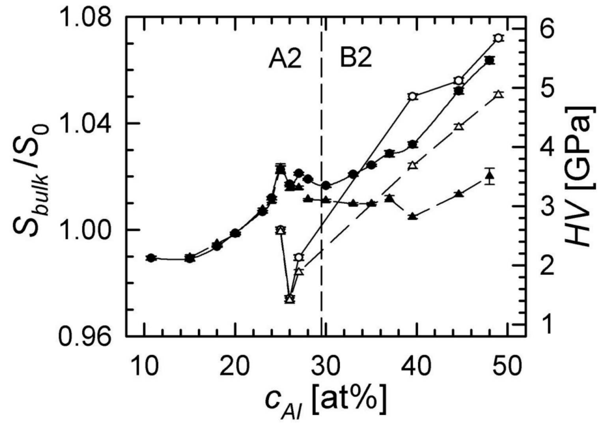

Fig. 5. Normalised S_{bulk} parameter and microhardness HV plotted against Al content, c_{Al}: Empty symbols — S_{bulk}, filled symbols — HV; circles — quenched alloys, triangles — annealed alloys (520 °C per 1h). Lines were drawn just to guide eyes.

In Fig. 5, we have also plotted the normalised S_{bulk} parameters for comparison. Note that the non-monotonicity exhibited in the figure by HV closely coincides with that of S_{bulk}, pointing out to a common cause of both effects — intermetallic phases formed depending on Al content. The behaviour of HV in the whole range of c_{Al} (called as the total hardness $\mathrm{HV_{tot}}$) should thus be described by the two mechanisms in the following way

$$\mathrm{HV_{tot}} = \mathrm{HV}_c\left(c_{\mathrm{Al}}\right) + \mathrm{HV_V}\left(c_{\mathrm{V}}\right). \tag{2}$$

The first term in above equation, $\mathrm{HV}_c(c_{\mathrm{Al}})$, expresses hardening controlled by Al content. In turn the second term, $\mathrm{HV_V}(c_{\mathrm{V}})$, is about the additional hardening induced by quenched-in vacancies. Due to low vacancy concentration, the vacancy-induced hardening is too small in alloys with $c_{\mathrm{Al}} < 27$ at%, leaving likely the anti-phase boundaries to be the main contribution to hardness in this region of Al concentrations. For c_{Al} above 30 at%, both hardening mechanisms become important. It seems plausible to assume that after annealing at 520 °C for 1 h an overwhelming majority of vacancies were already annealed out and, hardening controlled by Al content is not significantly influenced by annealing, i.e., the hardness values measured for the annealed alloys approximate sufficiently the $\mathrm{HV}_c(c_{\mathrm{Al}})$ term in (2). Under such assumptions, the $\mathrm{HV_V}(c_{\mathrm{V}})$ can be extracted as the difference between the total hardness for quenched and annealed alloys, namely

$$\mathrm{HV_V}\left(c_{\mathrm{V}}\right) \approx \mathrm{HV}_{\mathrm{tot}}^{(q)} - \mathrm{HV}_{\mathrm{tot}}^{(a)}, \tag{3}$$

where superscripts q and a distinguish quenched and annealed alloys, respectively.

Quenched-in vacancies are obstacles pining dislocations. In this case, $\mathrm{HV_V}(c_{\mathrm{V}})$ can be written [13] as

$$\mathrm{HV_V}\left(c_{\mathrm{V}}\right) = \mathrm{HV_V^{(0)}} + 6\mu\gamma\sqrt{c_{\mathrm{V}}}, \tag{4}$$

where $\mu \approx 100$ GPa is the shear modulus of Fe–Al [14], $\gamma < 1$ stands for the strength of vacancy–dislocation interaction and $\mathrm{HV_V^{(0)}}$ is the hardness at zero c_V.

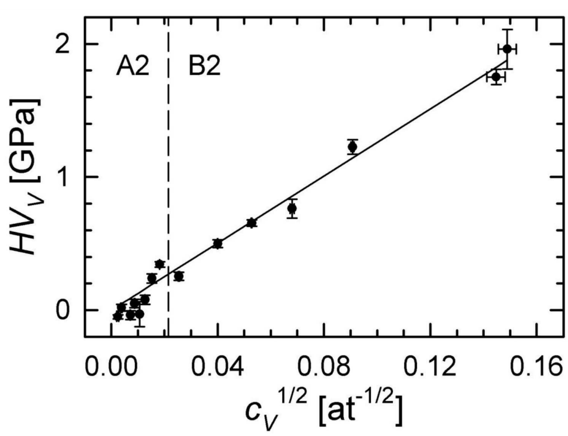

Fig. 6. Correlation between microhardness and vacancy concentration. See the text for further explanations.

The hardness data expressed in Fig. 5 as function of Al content could be converted into to the dependence on vacancy concentration c_{V}. This can be done using the VEPAS results of Fig. 4 as calibration points for the c_{V}-scale. Correlation of the $\mathrm{HV_V}(c_{\mathrm{V}})$ evaluated from the measured total hardness values using (3), is displayed on Fig. 6 against $\sqrt{c_{\mathrm{V}}}$. The solid line in the figure represents the $\mathrm{HV_V}(c_{\mathrm{V}})$-values calculated inserting $\mathrm{HV_V^{(0)}} \approx 0$ and $\gamma \approx 0.2$ into (4). Indeed, approaching the $\mathrm{HV_V^{(0)}}$ to zero may be expected. The γ-value, i.e., the slope of the line is about twice lower, yet of the same order, as that obtained for similar Fe–Al alloys in [13], supporting thus the above considerations.

4. Conclusions

The results of the present work can be summarised as follows:

1. The concentrations of vacancies in a series of Fe–Al alloys with different Al contents (18 to 49 at% Al), quenched from 1000 °C to room temperature, were estimated from positron back-diffusion study using the slow-positron beam technique. The concentration of quenched-in vacancies was found to strongly grow with increasing Al content.
2. Microhardness data and bulk S parameters, obtained for Fe–Al alloys with different Al content, exhibited non-monotonic behaviour in dependence on Al content around $c_{\mathrm{Al}} \approx 26$ at%.
3. Vacancy concentration data were correlated with microhardness measurements, which allowed to conclude that (a) hardening of Fe–Al alloys with low Al content (< 27 at%) is likely caused mainly by anti-phase boundaries and, (b) an additional mechanism, viz., vacancy-induced hardening, contributes to hardening in the Fe–Al alloys with higher Al content (> 30 at%).

Acknowledgments

Support by the Charles University Grant Agency (project 1506119) is highly acknowledged.

References

[1] *Binary Alloy Phase Diagrams*, (2nd Ed.), Eds. T.B. Massalski, H. Okamoto, P.R. Subramanian, L. Kacprzak, ASM International, Materials Park (OH) 1990.

[2] K. Ho, R.A. Dodd, *Scr. Metall.* **12**, 1055 (1978).

[3] T. Liu, E.H. Lee, C.G. McKamey, *Scr. Metall.* **23**, 875 (1989).

[4] H.E. Schaefer, B. Damson, M. Weller, E. Arzt, E.P. George, *Phys. Status Solidi (a)* **160**, 531 (1997).

[5] J. del Rio, N. de Diego, J.A. Jiménez, C. Gómez, *Intermetallics* **18**, 1306 (2010).

[6] O. Melikhova, J. Cizek, J. Kuriplach, I. Prochazka, M. Cieslar, W. Anwand, G. Brauer, *Intermetallics* **18**, 592 (2010).

[7] J. Cizek, F. Lukac, O. Melikhova, I. Prochazka, R. Kuzel, *Acta Mater.* **59**, 4068 (2011).

[8] J. Cizek, F. Lukac, I. Prochazka, R. Kuzel, Y. Jiraskova, D. Janickovic, W. Anwand, G. Brauer, *Physica B* **407**, 2659 (2012).

[9] F. Lukac, J. Cizek, I. Prochazka, Y. Jiraskova, D. Janickovic, W. Anwand, G. Brauer, *J. Phys.: Conf. Ser.* **443**, 012025 (2013).

[10] W. Anwand, G. Brauer, M. Butterling, H.R. Kissener, A. Wagner, *Defect Diffus. Forum* **331**, 25 (2012).

[11] A. van Veen, H. Schut, J. de Vries, R.A. Hakvoort, M.R. Ijpma, *AIP Conf. Proc.* **218**, 171 (1990).

[12] J. Kuriplach, *Phys. Procedia* **35**, 69 (2012).

[13] Y.A. Chang, L.M. Pike, C.T. Liu, A.R. Bilbrey, D.S. Stone, *Intermetallics* **1**, 107 (1993).

[14] A. Wolfenden, M. Harmouche, *J. Metals* **35**, 90 (1983).